Journal of Research and Applications in Mechanical Engineering
ISSN: 2229-2152 (Print); 2697-424x (Online)
(2025) Vol. 13, No. 3, Paper No. JRAME 25-13-036
[DOI: 10.14456/ jrame.2025.36]

Research Article

Verification of Density Based Solver in OpenFOAM for High-Speed Inviscid Compressible Flow Analysis

P. Kamma[1, 5]
K. Loksupapaiboon[2, 5]
J. Phromjan[3, 5]
C. Suvanjumrat[4, 5,*]
[1] *Department of Mechanical and Manufacturing Engineering, Faculty of Science and Engineering, Kasetsart University, Chalermphrakiat Sakon Nakhon Province Campus, Sakon Nakhon 47000, Thailand*
[2] *Department of Maritime Engineering, Faculty of International Maritime Studies, Kasetsart University Sriracha Campus, Chonburi 20230, Thailand*
[3] *Department of Mechanical Engineering, Faculty of Engineering, King Mongkut's University of Technology Thonburi, Bangkok 10140, Thailand*
[4] *Department of Mechanical Engineering, Faculty of Engineering, Mahidol University, Nakhon Pathom 73170, Thailand*
[5] *Laboratory of Computer Mechanics for Design (LCMD), Department of Mechanical Engineering, Faculty of Engineering, Mahidol University, Nakhon Pathom, 73170, Thailand*

Received 17 August 2024
Revised 17 December 2024
Accepted 18 December 2024

Abstract:
Computational Fluid Dynamics (CFD) has become essential for modeling and analyzing high-speed compressible flows around complex geometries. However, the utility of this tool is compromised if it is unreliable. This study examines the performance of RhoCentralFoam, a density-based solver in the open-source CFD software OpenFOAM, which utilizes the Kurganov-Noelle-Petrova (KNP) central upwind scheme for numerical flux calculations. RhoCentralFoam was validated by comparing its results against reliable analytical solutions and experimental data across various Mach numbers (Ma). The solver demonstrated an average error margin of less than 2% and performed effectively within the determined Ma range, depending on the geometrical model. Furthermore, the Van Albada and SFCD schemes exhibited no significant differences and were implemented without inducing instabilities in shock wave simulations. These findings confirm that RhoCentralFoam is a reliable CFD tool for simulating high-speed compressible flow phenomena, offering significant potential for future research and practical applications.

Keywords: *Shock wave, High-speed flow, CFD, OpenFOAM*

1. Introduction

In recent years, computational fluid dynamics (CFD) has become increasingly pivotal within the fields of aeronautics and astronautics, serving as a crucial tool for simulating and analyzing complex fluid dynamics phenomena [1-3]. This includes intricate behaviors like shock waves, expansion waves, and shock-shock interactions that occur in high-speed flows around complex geometries. Among the various numerical methods developed for such simulations, the finite volume method (FVM) has emerged as particularly adept at solving the hyperbolic conservation equations governing compressible flows at high speeds.

* Corresponding author: C. Suvanjumrat
E-mail address: chakrit.suv@mahidol.ac.th

Central to advancing these computational techniques is the accurate capture of shock waves, motivating ongoing refinement and innovation in discretization schemes within the FVM framework [4, 5]. For decades, the heat transfer enhancement by insertion of VG devices has been widely investigated both numerically and experimentally. The conjugate heat transfer and thermal stress in a circular tube with wire coiled inserted under a constant wall heat-flux was numerically investigated by Ozceyhan [8]. Chokphoemphun et al. [9] investigated numerically and experimentally the turbulent convection heat transfer in a circular tube inserted with winglet vortex generators (WVGs).

For instance, Zang et al. [11] conducted a comprehensive validation of the RhoCentralFoam solver by simulating supersonic-free jets under varying nozzle exit conditions. Their study highlighted the solver's robust performance, demonstrating close agreement with both qualitative observations and quantitative experimental data. OpenFOAM supports a diverse array of solvers tailored for simulating low-speed flows around intricate geometries as well as high-speed flows [12-14]. Recent enhancements to the RhoCentralFoam solver include the adoption of a third-order Runge-Kutta temporal discretization scheme, which has proven effective in improving computational efficiency while maintaining high accuracy [15]. In another validation effort, Alekseev et al. [16] analyzed an ensemble of numerical results obtained using five OpenFOAM solvers, each based on independent algorithms. The numerical tests were conducted for inviscid compressible flow around a cone at zero angle of attack. The norm of the approximation error and the error of the valuable functional (drag coefficient) were successfully estimated using an ensemble-based approach, which was confirmed by comparison with the etalon precise solution. Quintero et al. [17] provided novel experimental evidence on the correlation of supersonic gas jet instabilities with the oscillation of the filament in the melt-blowing and Cofiblas processes. They related these oscillations to the presence of shock waves and unsteadiness in the flow, offering valuable insights into the use of supersonic jets in the melt-blowing process as an effective approach for the formation of nanofibers. A thin 3D-axisymmetric model in OpenFOAM was tested by comparing the performance of different solvers, which were validated through flow visualization of the exit jet using digital holography.

The main goal of this work is to thoroughly validate the density-based solver RhoCentralFoam in OpenFOAM by simulating high-speed inviscid compressible flows across variously shaped geometric obstacles. The necessity to assess the solver's correctness and dependability for high-speed flow problems—which are crucial in astronautics and aeronautics—is what inspired this effort. Benchmarking RhoCentralFoam against analytical solutions and experimental data, finding performance constraints across a range of Mach numbers, and offering useful insights for its efficient deployment in engineering applications are the main contributions.

2. Governing Equation of High-Speed Flow

The high-speed flow is governed by differential equations that include the conservation of mass, momentum, and energy. These equations are written as follows:

$$\frac{\partial \rho}{\partial t} + \nabla \cdot (\rho \boldsymbol{U}) = 0 \tag{1}$$

$$\frac{\partial (\rho \boldsymbol{U})}{\partial t} + \nabla \cdot \big(\boldsymbol{U}(\rho \boldsymbol{U})\big) = -\nabla p + \nabla \cdot \tau \tag{2}$$

$$\frac{\partial (\rho E)}{\partial t} + \nabla \cdot \big(\boldsymbol{U}(\rho E)\big) = -\nabla \cdot (\boldsymbol{U} p) + \nabla \cdot (\tau \boldsymbol{U}) + k \nabla T \tag{3}$$

$$T = \frac{1}{C_v}\left(E - \frac{|\boldsymbol{U}|^2}{2}\right) \tag{4}$$

where τ is the viscous stress tensor, ρ, $\boldsymbol{U}$, T, k, p and E are density, velocity vector, temperature, conductivity, pressure, and total energy, respectively, and C_v is the specific heat of gas for constant volume.

3. Discretization Equations

The discretization of the FVM has been executed by integrating the above equations over the volume of an owner cell, as illustrated in Fig. 1. The owner cell, denoted as P, is enclosed by faces with outward-pointing vector ($\boldsymbol{S}_f$) normal to their surface. The neighbouring cell, labelled N, shares a common face with the owner cell, and a vector $\boldsymbol{d}$ connects the centroids of cells P and N. Additionally, the vector $\boldsymbol{d}_{fN}$ links the centre of the shared face to the centroid of the neighbouring cell.

3.1 Convective term

The convective term in equations (1)-(3) is treated using a differencing scheme. The discretization process involves integrating over a control volume and linearizing the equations, which can be expressed as follows:

$$\int \nabla \cdot (\boldsymbol{UW}) d\forall = \sum \emptyset_f \boldsymbol{W}_f \tag{5}$$

and $\boldsymbol{W} = \rho = \rho \boldsymbol{U} = \rho E,\ \boldsymbol{S}_f \cdot \boldsymbol{U}_f = \emptyset_f$ (6)

where $\boldsymbol{W}$ is a general tensor field and $\emptyset_{\mathrm{f}}$ is the volumetric flux.

For compressible flow, the KT and KNP methods [8, 9] are employed. The interpolation procedure is divided into two directions: outward and inward relative to the owner face cells. The direction f^+ aligns with $+\boldsymbol{S}_f$, while the direction f^- aligns with $-\boldsymbol{S}_f$. The discretized equation for the convective term can be written as follows:

$$\sum \emptyset_f \boldsymbol{W}_f = \sum \left[\left(\alpha \emptyset_{f+} \boldsymbol{W}_{f+} \right) + \left((1-\alpha) \emptyset_{f-} \boldsymbol{W}_{f-} \right) + \omega_f \left(\boldsymbol{W}_{f-} - \boldsymbol{W}_{f+} \right) \right] \tag{7}$$

$$\alpha = \begin{cases} \dfrac{1}{2} & for\ KT\ method \\ \dfrac{\varphi_{f+}}{\varphi_{f+} + \varphi_{f-}} & for\ KNP\ method \end{cases} \tag{8}$$

$$\varphi_{f+} = max\left(c_{f+} \left| \boldsymbol{S}_f \right| + \emptyset_{f+}, c_{f-} \left| \boldsymbol{S}_f \right| + \emptyset_{f-}, 0 \right) \tag{9}$$

$$\varphi_{f-} = max\left(c_{f+} \left| \boldsymbol{S}_f \right| - \emptyset_{f+}, \quad c_{f-} \left| \boldsymbol{S}_f \right| - \emptyset_{f-}, 0 \right) \tag{10}$$

$$c_{f\pm} = \sqrt{\gamma R T_{f\pm}} \tag{11}$$

$$\omega_f = \begin{cases} \alpha max\left(\varphi_{f+}, \varphi_{f-} \right) & for\ KT\ method \\ \alpha(1-\alpha)\left(\varphi_{f+} + \varphi_{f-} \right) & for\ KNP\ method \end{cases} \tag{12}$$

where α is weighting factor, c_f is the speed of sound of gas at the face, γ is adiabatic constant, R is gas constant, and ω_f is the diffusive volumetric flux.

3.2 Gradient term

The gradient term in Eq. (2), ∇p, is integrated over a control volume and interpolated as follows:

$$\int \nabla \cdot (\boldsymbol{W}) d\forall = \sum \boldsymbol{S}_f \boldsymbol{W}_f = \sum \left[\alpha \boldsymbol{S}_{f+} \boldsymbol{W}_{f+} + (1-\alpha) \emptyset_{f-} \boldsymbol{W}_{f-} \right] \tag{13}$$

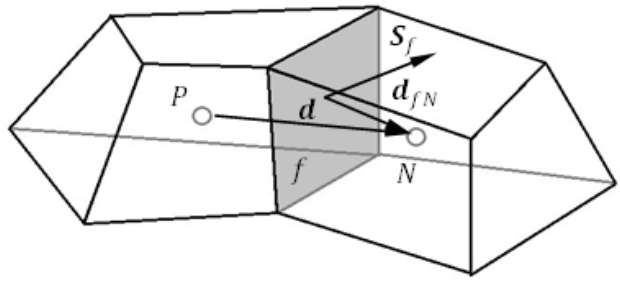

Fig. 1. Cell structure of finite volume method.

3.2 Laplacian term

The Laplacian term, with the diffusion coefficient Γ, is discretized. It is integrated over a control volume and interpolated as follows:

$$\int \nabla \cdot (\Gamma \nabla \boldsymbol{W}) d\forall = \sum \Gamma_f \boldsymbol{S}_f \cdot (\nabla \boldsymbol{W}_f) \tag{14}$$

$$\boldsymbol{S}_f \cdot (\nabla \boldsymbol{W}_f) = \left(\frac{|\boldsymbol{S}_f|^2}{\boldsymbol{S}_f \cdot \boldsymbol{d}} \right) (\boldsymbol{W}_N - \boldsymbol{W}_P) + \left(\boldsymbol{S}_f - \frac{|\boldsymbol{S}_f|^2}{\boldsymbol{S}_f} \right) \cdot (\nabla \boldsymbol{W})_f \tag{15}$$

4. Shock Wave Models

Three favourite examples—oblique shock waves, reflecting shock waves, and bow shock waves—are used to evaluate the capabilities of the RhoCentralFoam solver.

4.1 Oblique shock wave

Figure 2 presents a comprehensive schematic and the associated cell structure to illustrate and simulate the oblique shock wave phenomenon. In this scenario, a supersonic inviscid fluid flows around a 40° cone body, encountering a shock wave that forms at an angle to the incoming flow direction upon reaching the leading edge of the cone. This interaction results in a pronounced redirection of the fluid's flow path, along with substantial compression and heating within the flow field. The cell structure of the oblique shock wave exhibits X-axis symmetry and is constructed using hexahedral cells. The number of cells is determined by conducting a grid independence test. The boundaries of this structure include the inlet, outlet, symmetry, open, and wedge surface.

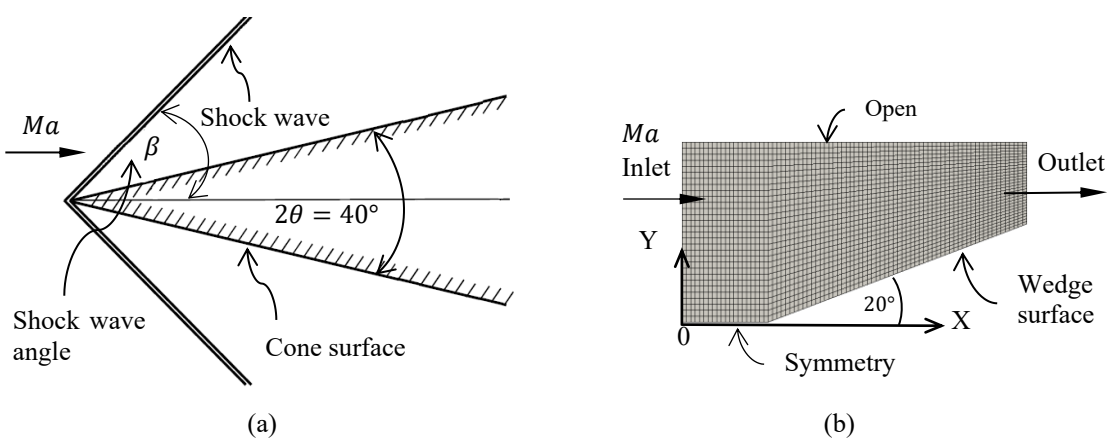

Fig. 2. Oblique shock wave: (a) schematic and (b) cell structure.

4.2 Reflecting shock wave

Figure 3 presents a comprehensive schematic of a reflecting shock wave, also known as a rebound shock wave. In this scenario, an inviscid fluid flows through a cavity channel containing a wedge-shaped object. Initially, a shock wave forms at the nose of the wedge due to its cone shape, similar to the previously observed oblique shock wave. However, this shock wave encounters the solid cavity wall, it produces an incident shock wave, resulting in a reflecting shock wave that travels back into the fluid stream. This reflected shock wave moves downstream, where the flow immediately next to the wall must remain parallel to the wall. This interaction can create intricate flow patterns and secondary shock waves throughout the flow field. In the CFD domain, hexahedral cells were employed to ensure high-fidelity aerodynamic simulations. Furthermore, boundary conditions were carefully applied to accurately represent the physical scenarios, including inlet, outlet, symmetry, wall, and wedge body boundaries.

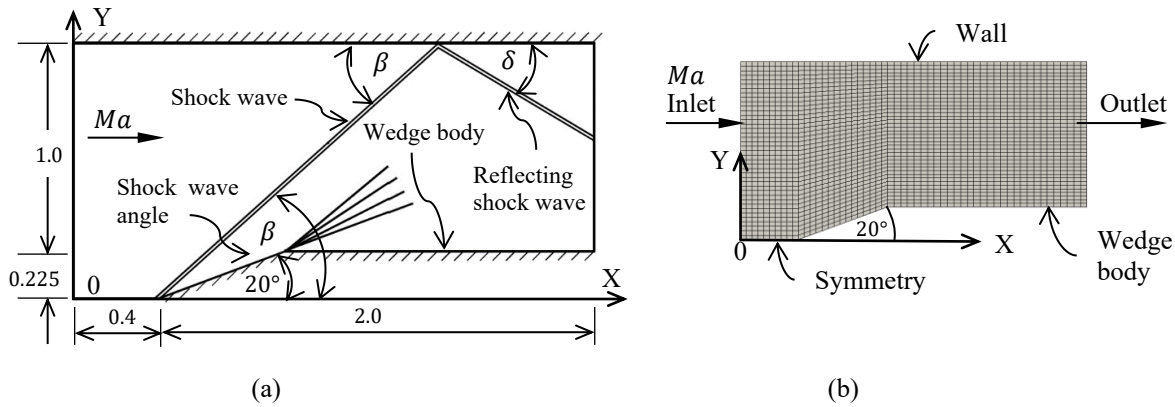

Fig. 3. Reflecting shock wave: (a) schematic and (b) cell structure.

4.3 Bow shock wave

Figure 4 illustrates a detailed schematic of a bow shock wave, referred to as a bow shock. Similar to the oblique shock wave, this phenomenon arises when an object moves through a fluid medium at supersonic speeds. The bow shock's characteristic concave shape is defined by the blunt nose of the object, which causes rapid compression and heating of the surrounding fluid. In the CFD domain, hexahedral cells were used to align with the bow shock, ensuring accurate simulation results. The boundary conditions for this domain included inlet, outlet, symmetry, and cylinder boundaries.

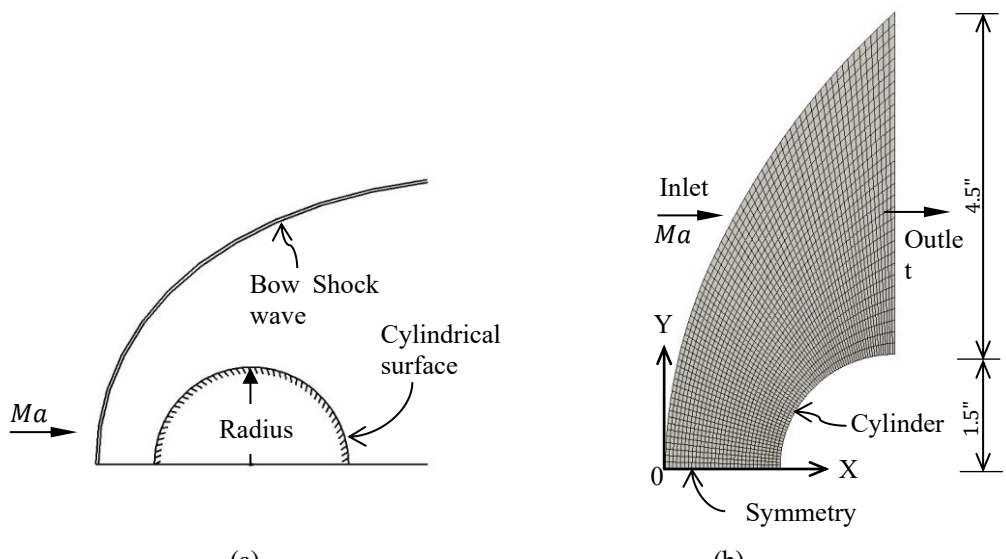

Fig. 4. Bow shock wave: (a) schematic and (b) cell structure.

4.4 Boundary conditions

Velocity and pressure were assigned at the boundaries. At the inlet, the velocity was set to a fixed value calculated based on the inlet Ma. At the outlet face, a zero-gradient condition with a backflow boundary prevention setup from OpenFOAM was implemented to prevent spurious reflections. For the obstacle walls, such as the cone, wedge, and cylindrical surfaces, a slip condition was applied to the velocity, allowing tangential movement along the surface. The temperature and pressure at the inlet were set to fixed values. While at the outlet, a zero-gradient condition was maintained for both temperature and pressure. Additionally, a symmetry condition was enforced at the symmetry face to simulate reflective symmetry in the flow field.

A gas with a specific heat ratio (γ) of 1.4, an initial pressure of 1, and an initial temperature of 1 was used for the shock wave simulations. Furthermore, the speed of sound was simplified to 1 using the relationship $R = \gamma^{-1} = 0.714$.

5. Result and Discussion

The accuracy of the RhoCentralFoam solver in OpenFOAM software depends on cell size, numerical schemes, and shock wave visibility. These factors are described and discussed in the following sections.

5.1 Grid independence

Figure 4 displays the simulation results via the Ma contour. In this study, the inlet flow was set to Ma 3. The oblique shock wave is clearly visible and angled to the cone surface. The Ma contour revealed two distinct triangular regions above the cone surface: a red region and a blue region. The transitional layer between these regions or the shock wave, exhibited Ma values between 1.9 and 3.0. The thickness of this layer was influenced by the cell size or the number of cells. To test this assumption, five levels of fine cells were used: 800, 3,200, 12,800, 51,200, and 208,800 cells, corresponding to cell sizes of 0.05, 0.025, 0.0125, 0.00625, and 0.003125 m, respectively. Each grid resolution was named as Grid1 through 5.

To investigate the effects of cell size, Ma values were plotted along the line normal to the 40-degree shock wave. The Ma range of the shock wave served as the criterion for determining the appropriate cell number or cell size. A cell number of 51,200 resulted in a shock wave thickness of 0.02379 m, while a cell number of 208,800 yielded a thickness of 0.01753 m. The cell number of 208,800 produced a shock wave thickness 4% less than that of 51,200. Conversely, a cell number of 12,800 resulted in a shock wave thickness of 0.05933 m, which was 5.6% greater than that of 51,200. Therefore, a cell number of 51,200 is recommended for simulating the oblique shock wave as it offers a balance between computational efficiency and shock wave thickness, closely matching the results of using 208,800 cells but with reduced computation.

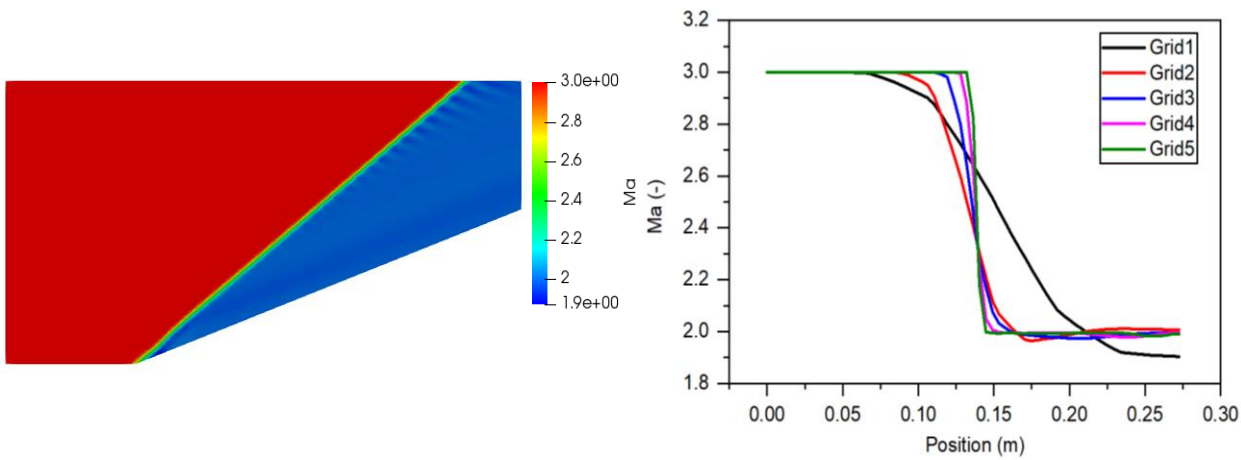

(a) (b)

Fig. 5. Results of the oblique shock wave at Ma = 3: (a) Ma contour and (b) grid independence test.

5.2 Schemes

The oscillatory behavior observed in the blue zone behind the shock wave, as shown in Figure 5(a), indicates numerical instability. This instability is likely to be present in both the reflecting shock wave model and the bow shock wave model. Despite attempts to reduce cell size to mitigate these oscillations, they persist even with the finest cells. Consequently, an investigation into the discretization of schemes for convective flux (KT and KNP) was conducted.

In the previous grid independence test, the Van Leer interpolation scheme was employed. Building on this, the current study examines the oblique shock setting using the KT convective flux differencing scheme. Four convective interpolation schemes available in OpenFOAM including Upwind, Self-filtered Central Differencing (SFCD), VanLeer01, and VanAlbada were directly compared to the Van Leer scheme. Each scheme was tested under identical numerical conditions to ensure consistency with the previously established parameters.

As depicted in Figure 6, the original Van Leer interpolation scheme shows oscillations near the upper part close to the outlet boundary, as previously observed. These oscillations can be mitigated by employing alternative schemes such as Self-filtered Central Differencing (SFCD), Upwind, and Van Albada. While the first-order Upwind scheme effectively eliminates oscillations, it produces a noticeably thicker shock wave, indicating a trade-off between numerical stability and shock resolution. Additionally, the VanLeer01 scheme introduces more oscillations, suggesting its unsuitability for supersonic and hypersonic flow simulations. The results from the Van Albada and SFCD schemes exhibit no significant differences and can be implemented without instability for this type of simulation.

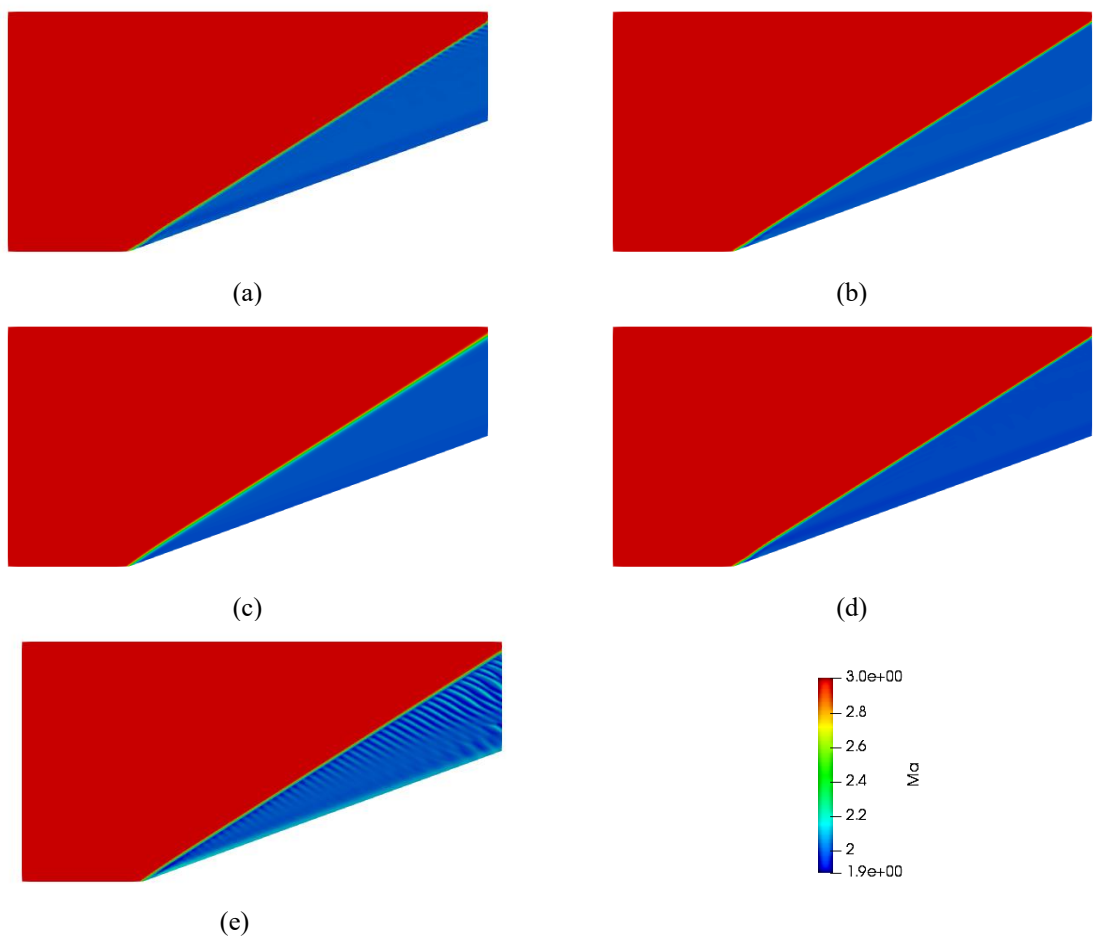

Fig. 6. Computation of an oblique shock wave computing at Ma =3 using various schemes: (a) Vanleer, (b) SFCD, (c) Upwind, (d) VanAlbada, and (e) Vanleer01.

5.3 Validation and limitation

The simulated results of the oblique shockwave are depicted using stream tracers with velocity contours to visualize the velocity distribution and shock wave direction at Ma 5, as shown in Fig. 7. The incoming stream flowed horizontally from the inlet and impacted the oblique wedge surface, causing the stream tracers to deflect upward toward the main flow. This interaction reoriented the high-speed flow, characteristic of supersonic and hypersonic conditions, resulting in the formation of an oblique shock wave. This shock wave was represented as a distinct thin gradient layer between the red and blue contours. The transition in velocity and direction across the shock wave was apparent, with the post-shock flow closely aligning with the wedge surface.

The analytic solution for the oblique shock wave angle at various Ma [18] is given as follows:

$$\theta = \frac{2cot\beta(Ma^2 sin^2\beta - 1)}{2 + M^2(\gamma + cos2\beta)} \tag{16}$$

where θ is the deflection angle, β is the wave angle and γ is a specific heat ratio.

The simulation and analytical solution demonstrated that the shock wave angle decreased as the Ma increased. Additionally, the wave angle stabilized at approximately 25 degrees at high Ma. The solver showed excellent agreement with the analytical solution, with an average error of less than 0.75% RhoCentralFoam solver effectively computes the oblique shock wave for Ma ranging from 2 to 12. However, beyond this range, the solver encounters difficulties completing simulations, even with grid refinement and adjustments to simulation conditions. The oblique shock wave angle obtains from CFD simulation using the RhoCentralFoam solver derives from Eq. (17), yielding an R^2 value of 0.98.

$$\beta = -0.12Ma^3 + 3.10Ma^2 + 24.35Ma + 88.93 \tag{17}$$

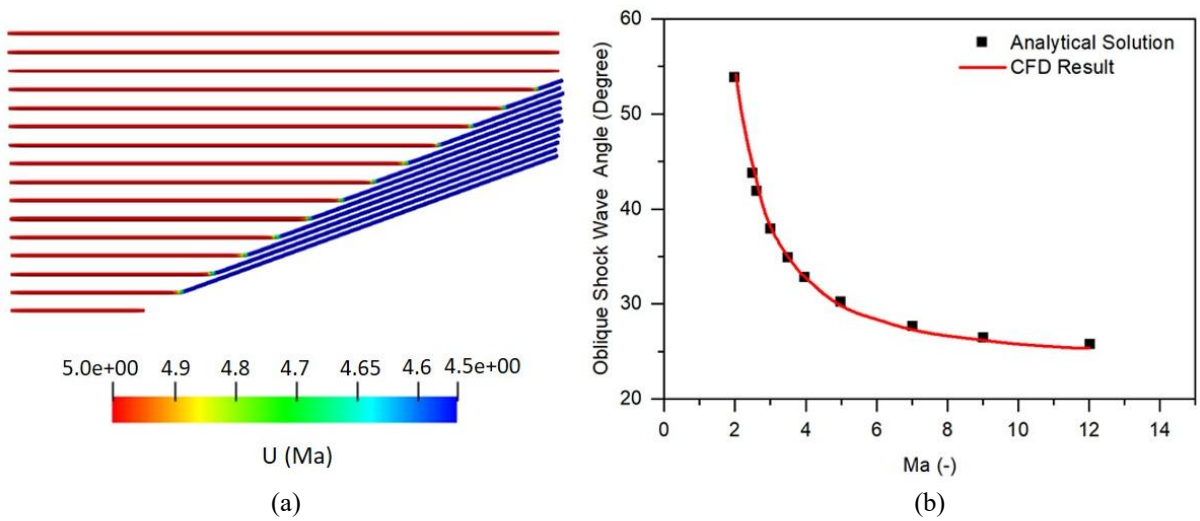

Fig. 7. CFD results of the oblique shock wave model: (a) Stream tracers and velocity contours, and (b) Comparison with the analytical solution.

Figure 8 illustrates the simulated reflecting model, where the incoming stream flows horizontally from the inlet, colliding with the wedge surface and generating an oblique shock wave. However, the downstream oblique shock wave subsequently impinges upon the upper wall. The simulation reveals that rather than dissipating, the impinging wave generates a second shock wave, known as the reflected shock wave. At this stage, velocity changes occur across the reflected shock wave, and the stream tracers behind it tend to align parallel to the upper surface. The reflecting shock wave angles, when compared to the analytical solution [18] at various Ma ranging from 3 to 6, showed an average error of less than 1.1%. Beyond this range, the oblique shock wave generated by the wedge surface does not interact with the upper wall. Additionally, this work evaluates the solver's performance, demonstrating its capability

to handle Ma up to 13. The reflecting shock wave angle obtained from the CFD simulation using the RhoCentralFoam solver is derived from Eq. (18), yielding an R^2 value of 0.97.

$$\delta = 152.5Ma^{-1.365} \tag{18}$$

Figure 9 illustrates the bow shock wave simulation at Ma 6.45. The incoming stream flows horizontally from the inlet and impacts a blunt, spherical object, resulting in the formation of the bow shock wave. This shock wave appears as a thin layer near the point of abrupt streamline redirection. At the sphere's centreline, the upstream flow remains perpendicular to the shock wave. However, as the distance from the sphere increases, the shock wave gradually curves and weakens, eventually evolving into a Mach wave at substantial distances from the body. The bow shock wave simulation was compared with the shock wave position extracted from a Schlieren photograph [19]. The simulation closely matches the experimental data, achieving an R^2 value of 0.99. Additionally, this solver successfully completed the solution as the Ma increased to 40, indicating no limitations with this model.

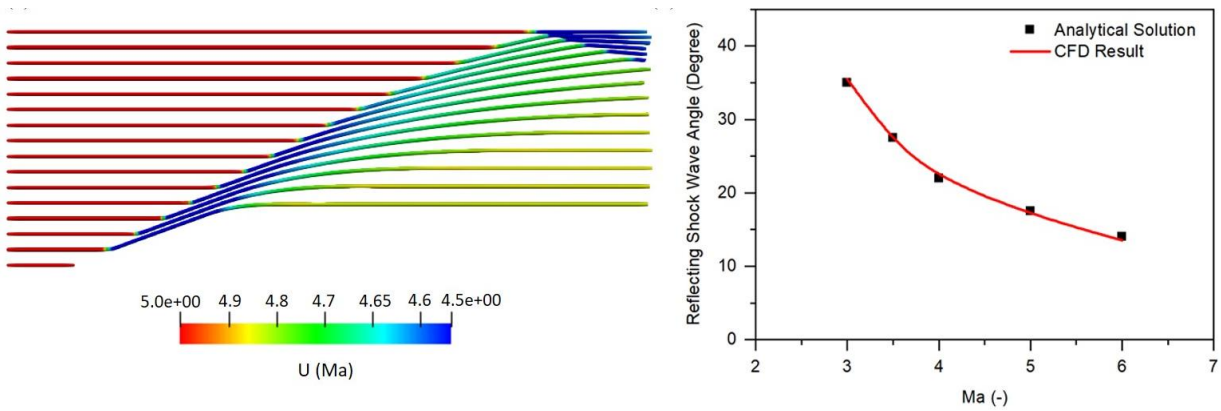

Fig. 8. CFD results of the reflecting shock wave model: (a) Stream tracers and velocity contours, and (b) Comparison with the analytical solution.

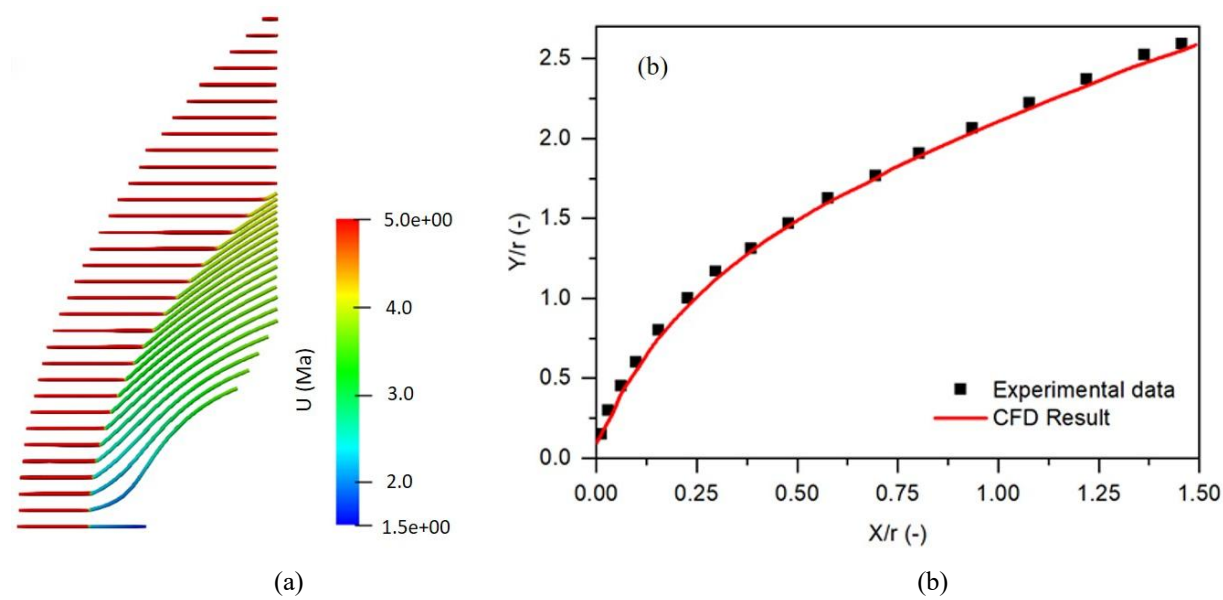

Fig. 9. CFD results of the bow shock wave model: (a) Stream tracers with velocity contours, and (b) Comparison with the experiment.

6. Conclusion

The density-based solver rhoCentralFoam, implemented in OpenFOAM was evaluated for high-speed inviscid compressible flow analysis. This solver utilized new Godunov-type central semi-discrete schemes, KT and KNP, for discretizing the convective term in the conservation equations. Three configuration models were conducted to assess the solver's performance. The key findings of this study are as follows:

1. The simulations of all three shock wave models using the KT and KNP schemes for the convective term discretization exhibited no significant differences in the results. Consequently, both schemes are suitable for high-speed flow simulations.
2. The interpolation schemes SFCD and Van Albada were found to be optimal for reconstructing T, $\boldsymbol{U}$, and ρ, as they produced results without oscillations. The first-order Upwind scheme, while preventing oscillations and providing rapid calculations, results in a thicker shock wave, indicating a trade-off between numerical stability and shock resolution. The Van Leer and VanLeer01 schemes were unsuitable due to significant oscillations, making them inappropriate for high-speed flow simulations.
3. RhoCentralFoam successfully completed simulations for Ma up to 12 and 13 for the oblique and reflecting shock wave models, respectively. No limitation was observed for the bow shock wave model, tested up to a Ma of 40, demonstrating the solver's capability and robustness. Therefore, RhoCentralFoam, as a compressible solver based on OpenFOAM, is a potent tool for investigating shock wave phenomena without requiring licensed software or extensive experimental setups.
4. The oblique and reflecting shock wave angles, corresponding to the Mach number (Ma), were proposed through equations exhibiting R^2 values of 0.98 and 0.97, respectively. These equations can be used to calculate the shock wave angles without the need for CFD simulations.

References

[1] Intano W, Kaewpradap A, Hirai S, Masomtob M. Thermal investigation of cell arrangements for cylindrical battery with forced air-cooling strategy. Journal of Research and Applications in Mechanical Engineering. 2020;8(1):11-21.

[2] Lahamornchaiyakul W, Kasayapanand N. Design and analysis of a novel vertical axis water turbine for power generation from water pipelines using k-epsilon and SST k-omega model. Journal of Research and Applications in Mechanical Engineering. 2023;11(2):1-19.

[3] Chaiyanupong J, Khajorntraidet C. Design and analysis of double element airfoil using RANS. Journal of Research and Applications in Mechanical Engineering. 2024;12(1):1-9.

[4] Chaichanasiri E, Suvanjumrat C. Simulation of three dimensional liquid-sloshing models using C++ open source code CFD software. Kasetsart Journal: Natural Science. 2012;46(6):978-995.

[5] Ruchayosyothin S, Konglerd P, Tamna S. The computational modelling in the prediction of flow past a rotating sphere at high Reynolds number. Journal of Research and Applications in Mechanical Engineering. 2022;10(1):1-14.

[6] Simon S, Mandal JC. A simple cure for numerical shock instability in the HLLC Riemann solver. Journal of Computational Physics. 2019;378:477-496.

[7] Chen SS, Cai FJ, Xue HC, Wang N, Yan C. An improved AUSM-family scheme with robustness and accuracy for all Mach number flows. Applied Mathematical Modelling. 2020;77:1065-1081.

[8] Kurganov A, Tadmor E. New high-resolution central schemes for nonlinear conservation laws and convection–diffusion equations. Journal of Computational Physics. 2000;23(3):707-740.

[9] Kurganov A, Noelle S, Petrova G. Semidiscrete central-upwind schemes for hyperbolic conservation laws and Hamilton-Jacobi equations. SIAM Journal on Scientific Computing. 2001;160:241-282.

[10] Greenshields CJ, Weller HG, Gasparini L, Reese JM. Semidiscrete central-upwind schemes for hyperbolic conservation laws and Hamilton-Jacobi equations. International Journal for Numerical Methods in Fluids. 2010;62:1-21.

[11] Zang B, Vevek US, Lim HD, New TH. An assessment of OpenFOAM solver on RANS simulations of round supersonic free jets. Journal of Computational Physics. 2018;28:18-31.

[12] Suvanjumrat C, Loksupapaiboon K. Improvement of thermal distribution in the rubber-glove former conveyor oven by OpenFOAM. Engineering Journal. 2020;24(2):109-120.

[13] Kamma P, Promtong M, Suvanjumrat C. Development of a reduced mechanism for methane combustion in OpenFOAM: A computational approach for efficient and accurate simulations. International Journal of Thermofluids. 2024;22:100654.

[14] Loksupapaiboon K, Suvanjumrat C. Curing analysis of rubber film on a hand-shaped former in the manufacturing of rubber gloves through novel OpenFOAM solver. International Journal of Heat and Fluid Flow. 2024;108:109476.
[15] Li S, Paoli R, D'Mello M. Scalability of OpenFOAM density-based solver with Runge–Kutta temporal discretization scheme. Scientific Programming. 2020;9083620.
[16] Alekseev AK, Bondarev AE, Kuvshinnikov AE. On uncertainty quantification via the ensemble of independent numerical solutions. Journal of Computational Science. 2020;42:101114.
[17] Quintero F, Doval AF, Goitia A, Vazquez R, Crespo K, Barciela R, Fernandez-Arias M, Lusquinos F, Otto A, Pou J. Analysis of the oscillations induced by a supersonic jet applied to produce nanofibers. International Journal of Mechanical Sciences. 2023;238:107826.
[18] Anderson JD Jr. Modern Compressible Flow with Historical Perspective. 3rd ed. New York: McGraw-Hill Education; 2003.
[19] Wieting AR. Experimental study of shock wave interference heating on a cylindrical leading edge. NASA Technical Memorandum. 100484.